Chapter 10
Metal Oxide Catalysts in Relation to Environmental Protection and Energy Conversion

Saburo Hosokawa and Teruki Motohashi

10.1 General Background for Environmental Protection and Energy Conversion

Global warming is becoming a serious problem, leading to an urgent need for efficient processes for the removal of harmful gases, as well as the development of renewable energy resources. The development of highly functional catalyst materials is therefore highly needed [1, 2]. Furthermore, from the viewpoint of resources and economy of platinum group metals (PGMs) such as Rh and Pd, it is also desired to develop catalyst materials that do not contain PGMs or reduce the use of PGMs minimized as much as possible [3–6]. Nowadays, base metal catalysts have drawn attention with researchers focusing on the development of metal oxides that exhibit excellent redox properties. This chapter introduces metal oxide catalysts that contribute to environmental protection and the effective utilization of methane. In particular, the chemical characteristics of CeO_2-based oxides with a fluorite-type structure and perovskite-type oxides are outlined from the perspective of the packing structure of O^{2-} ions. In addition, oxygen storage materials, which are applicable to various fields involving catalytic reactions, are introduced from the viewpoint of the structural changes associated with the insertion and extraction of O^{2-} ions. Finally, oxidative coupling on metal oxides, which contributes to the effective utilization of methane, is introduced.

S. Hosokawa (✉)
Faculty of Materials Science and Engineering, Kyoto Institute of Technology, Matsugasaki, Sakyo-ku, Kyoto 606-8585, Japan
e-mail: hosokawa@kit.ac.jp

T. Motohashi (✉)
Department of Material and Life Chemistry, Kanagawa University, 3-27-1, Rokkakubashi, Kanagawa-ku, Yokohama 221-8686, Japan
e-mail: t-mot@kanagawa-u.ac.jp

© The Author(s), under exclusive license to Springer Nature Singapore Pte Ltd. 2022

W. Ueda (ed.), *Crystalline Metal Oxide Catalysts*,
https://doi.org/10.1007/978-981-19-5013-1_10

10.2 CO and VOC Oxidations

10.2.1 Overview

Catalytic combustion is effective for removing CO and volatile organic compounds (VOCs). This process uses a catalyst material that purifies harmful gases to CO_2 and H_2O at temperatures typically below 300 °C. Such a procedure does not induce flame combustion and is much safer than simple combustion processes that ignite with a flame. The process is also advantageous for environmental protection because of the suppressed evolution of incomplete combustion products and thermal NO_x, which are formed by exposure to N_2 and O_2 in air at high temperatures. The use of PGMs is indispensable for improving catalytic activity in the low-temperature range [7], whereas many studies have been conducted on metal oxide catalysts without PGM species for catalytic combustion. Highly active metal oxide catalysts and their crystal structures have been the subject of many publications [8], including CeO_2-based oxides, perovskite-type oxides, and spinel-type oxides. In general, all catalyst materials utilize metal oxides containing elements with excellent redox properties.

This section begins by presenting the relationship between the redox ability of metal oxides and the reaction mechanisms, followed by the structural characteristics of each metal oxide for typical catalyst materials.

10.2.2 Reaction Mechanism (Mars-Van Krevelen Mechanism)

In the catalytic combustion on a PGM catalyst, adsorption of reaction substrates and activation of O_2 molecules are known to occur on the surface of PGM. That is, the catalytic reaction proceeds according to a reaction based on the Langmuir–Hinshelwood mechanism (or Eley–Rideal mechanism) (Fig. 10.1) [9]. Therefore, when designing supported PGM catalysts, the high dispersion of PGM particles and the control of the electronic state by forming PGM alloy nanoparticles should be studied [10, 11]. In contrast, regarding metal oxide catalysts, the combustion mechanism involving lattice oxygen based on the Mars-van Krevelen (MvK) mechanism has become common [12–14]. Here, CO oxidation (Eqs. 10.1 and 10.2) is presented as an example to explain this reaction mechanism. First, CO reacts with lattice oxygen (O_L) at the oxide surface to generate CO_2 followed by an O_2 molecule filling the generated oxygen vacancies (V_O).

$$CO + O_L \rightarrow CO_2 + V_O \tag{10.1}$$

$$O_2 + V_O \rightarrow 2O_L \tag{10.2}$$

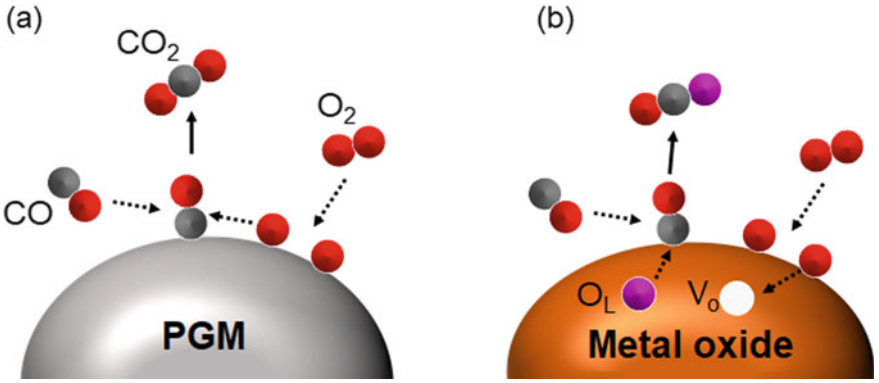

Fig. 10.1 CO oxidation based on **a** Langmuir–Hinshelwood and **b** Mars-van Krevelen mechanisms

The transfer of lattice oxygen in the metal oxide is a key step in this reaction mechanism. It is therefore preferable to optimize the redox properties of the constituent metal species when designing metal oxide catalysts.

10.2.3 CeO_2-Based Materials

Ce^{4+} ions contained in CeO_2 are easily reduced to Ce^{3+} and this redox plays a crucial role in the use of CeO_2 as a catalyst [15]. CeO_2 crystallizes in a fluorite-type structure in which Ce^{4+} ions form a face-centered cubic lattice, with O^{2-} ions occupying the tetrahedral voids (Fig. 10.2). In other words, the O^{2-} ions compose a primitive cubic structure, with Ce^{4+} ions located at the body-centered sites. In the case of transition-metal oxides such as NaCl-type MnO and spinel-type Co_3O_4, the ionic radius of transition metals such as Fe^{3+} (0.55 Å) and Co^{3+} (0.545 Å) is much smaller than that of the O^{2-} ion (1.40 Å). This difference in radius results in a close-packed structure composed of the O^{2-} ions (Fig. 10.3) where the transition metal ion occupies the tetrahedral or octahedral voids formed by the O^{2-} ions. For CeO_2, on the other hand, the size of the Ce^{4+} ions (0.97 Å) is larger than that of the transition metal ions, indicating that the O^{2-} ions do not form a close-packed structure and prefer a primitive cubic structure instead. This characteristic packing structure of the O^{2-} ions facilitates their fast diffusion in the CeO_2 crystal lattice, even though their diffusion depends on the defect chemistry as well [16]. Thus, the redox property of cerium and the transfer ability of O^{2-} ions in CeO_2 are promising features for the above-mentioned MvK mechanism.

Many studies on combustion catalysts using CeO_2 exist, analyzing the correlation between the oxygen release property and combustion activity and reporting that the reactivity of lattice oxygen in CeO_2 was drastically improved by PGM loading [17–19]. CeO_2 is often combined with CuO or Co_3O_4 as a PGM-free catalyst [20–23]; the

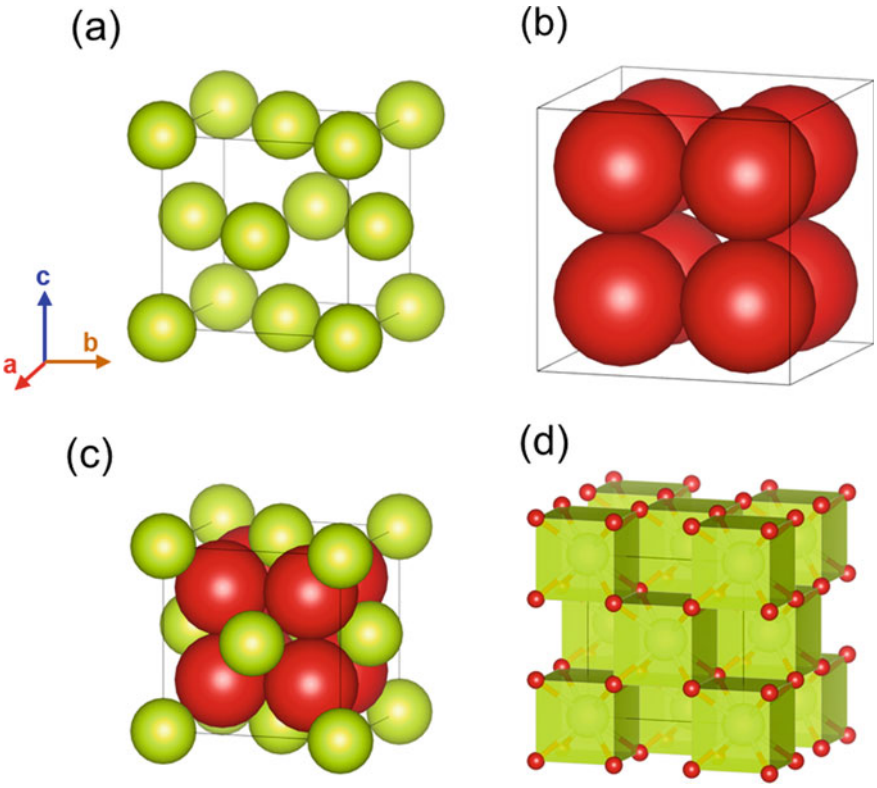

Fig. 10.2 Crystal structure of CeO_2 with a fluorite structure. **a** Positions of Ce ions and **b** O^{2-} ions in the unit cell. **c** Structure constructed by Ce and O^{2-} ions. **d** Crystal structure providing a clear view of the coordination environment of the Ce ions. Panels (**a–c**) are shown based on actual ionic radii: yellow balls, Ce^{4+} ions; red balls, O^{2-} ions. The schematic crystal structures in this chapter are drawn by VESTA program (K. Momma and F. Izumi. J. Appl. crystallogr., 2011, 44, 1272)

formed composites exhibit high mobility of lattice oxygen, resulting in high catalytic activity for VOCs combustion. Most of these reaction behaviors are explained by the MvK mechanism. Meanwhile, the reactivity of lattice oxygen in CeO_2 is closely related to the exposed crystal plane. Theoretical studies indicate that the (110) and (100) planes have high catalytic activity, emphasizing the importance of morphology control of the CeO_2 nanoparticles [24, 25]. In fact, rod-shaped CeO_2 particles, in which (110) planes are preferentially exposed, exhibit high VOC combustion activity. Furthermore, it has been demonstrated that the catalytic oxidation of CO with rod-shaped CeO_2 proceeds at lower temperatures than with cubic or octahedrally shaped CeO_2 grains.

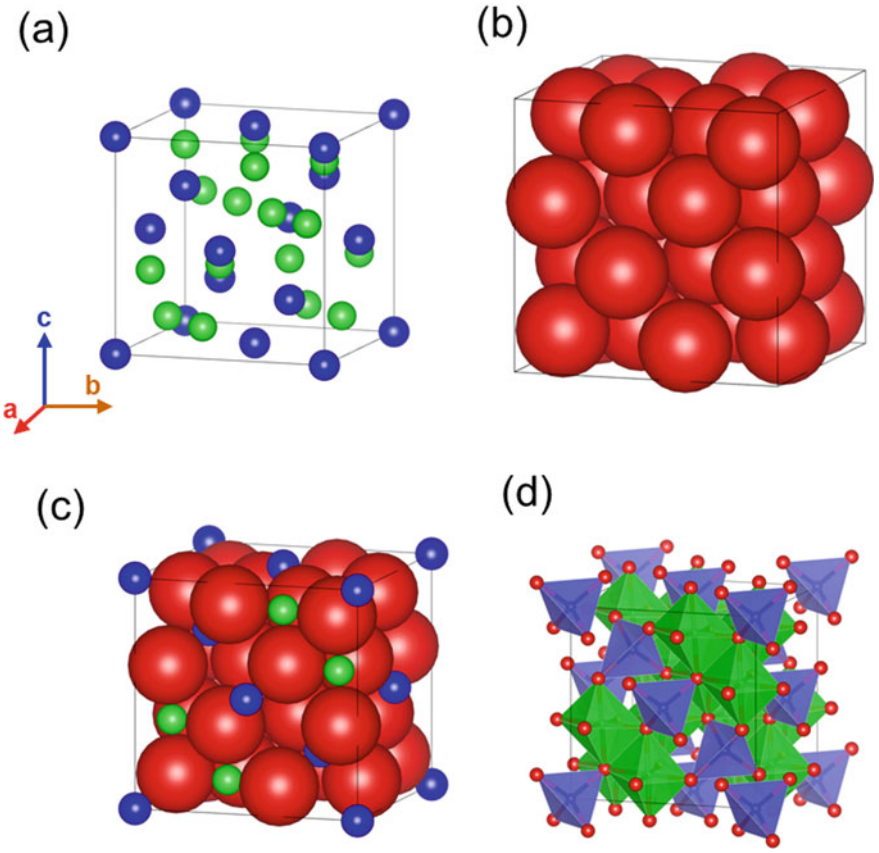

Fig. 10.3 Crystal structure of Co_3O_4 with a spinel structure. **a** Positions of Co ions and **b** O^{2-} ions in the unit cell. **c** Structure constructed by Co and O^{2-} ions. **d** Crystal structure providing a clear view of the coordination environment of the Co ions. Panels (**a–c**) are shown based on actual ionic radii: blue balls, Co^{2+} ions; green balls, Co^{3+} ions; red balls, O^{2-} ions

10.2.4 Perovskite Oxides

Since 3d transition metals can adopt a wide range of valence states, transition metal-based oxide catalysts have been extensively studied for combustion reactions from the perspective of the redox ability of their metal species. Many reports exist on perovskite oxides, which are generally represented by the chemical formula ABO_3 [6, 26–28]. The A site of the perovskite structure is often composed of alkali metals, alkaline-earth metals, or rare-earth metals, whereas the B site contains transition metals. Unlike the close-packed structure of the O^{2-} ions in NaCl-type and spinel-type transition metal oxides described in the previous section, the A-site cation and O^{2-} ion form a close-packed structure. This is due to the ionic radius of the A-site cation in the perovskite structure being similar to that of the O^{2-} ion (Fig. 10.4).

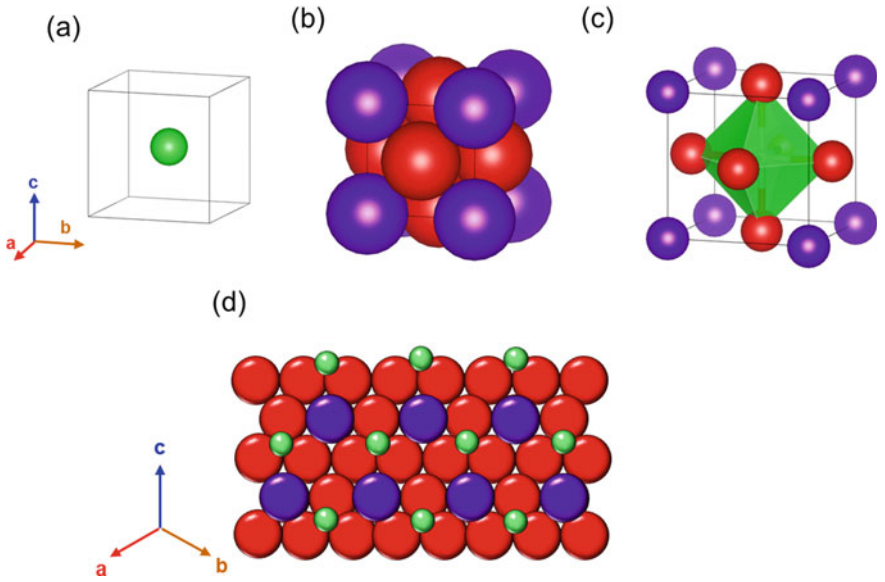

Fig. 10.4 Crystal structure of ABO_3 with a perovskite structure. **a** Positions of B ions and **b** A ions, and O^{2-} ions in the unit cell. **c** Crystal structure with a clear view of the coordination environment of the B ion. **d** Relationship between the A and B ions. Panels (**a**, **b**, and **d**) are shown based on actual ionic radii: Purple balls, A ions (alkali or alkali-earth elements); brown balls, B ions (transition metal elements); red balls, O^{2-} ions

The B-site metal occupies the octahedral interstice consisting of O^{2-} ions. The ideal perovskite structure belongs to the cubic system, whereas many perovskite oxides are known to exhibit tetragonal or orthorhombic distortion according to the ionic radii of the metals occupying the A and B sites.

An important advantage of perovskite oxides from the viewpoint of catalyst material design is that the constituent elements of the A and B sites can be chemically substituted. For example, partial substitutions of the A site can adjust the valence state of the B-site element or promote the formation of oxygen vacancies according to the charge balance. The substitution of Sr^{2+} for La^{3+} in $La^{3+}Co^{3+}O_3$ is expected to induce oxygen defects and control the Co valence state. In addition, partial substitutions of the B site can modulate the redox capacity of the B-site cation and the mobility of the O^{2-} ions. The possibility of adjusting these properties through the choice of dopants is a critical factor for efficient catalytic reactions based on the MvK mechanism.

Among the La-based transition metal oxides, $LaM^{3+}O_3$, $LaMnO_3$, and $LaCoO_3$ are known to be active in CO oxidation [27]. Furthermore, the Sr-for-La-substituted material, $La_{1-x}Sr_xMnO_3$, exhibits excellent catalytic performance. There are many other reports on the development of combustion catalysts based on perovskite structures, and the reader is referred to various review articles for further detail [6, 28, 29].

10.2.5 Other Metal Oxides

One of the most representative materials as a metal oxide catalyst for CO oxidation is Co_3O_4 with a spinel-type structure [30]. The Co_3O_4 catalyst having a rod-like morphology shows excellent catalytic ability even at room temperature. In general, the spinel structure presents a composition of AB_2O_4, where the A cation occupies the tetrahedral interstice formed in the close-packed structure of the O^{2-} ions, and the B cation occupies the octahedral interstice. The A and B cations are typically divalent and trivalent, respectively. For example, when clarifying the valence of Co species of Co_3O_4, it can be expressed as $Co^{2+}[Co^{3+}]_2O_4$. Since the 3d transition metal can be distributed at the A and B sites in the spinel structure, binary and ternary mixed oxides can be easily obtained by substituting various elements. Furthermore, it is possible to adjust the redox ability by selecting the metal species and multicomponent spinel oxides exhibit excellent catalytic ability. For example, spinel-type $CoMn_2O_4$ shows a higher ability to release lattice oxygen than a mixture of Co_3O_4 and MnO_x, a feature that is useful for toluene oxidation [31–33].

Other types of metal oxide catalysts are hexagonal rare-earth-iron mixed oxides ($REFeO_3$). $REFeO_3$ crystallizes in an orthorhombic perovskite structure with *Pbnm* being a stable form for all the rare-earth elements, while hexagonal $REFeO_3$ (*h*-$REFeO_3$) with $P6_3cm$ exists as a metastable phase [34]. In the unit cell of *h*-$REFeO_3$, layers of iron ions and RE ions are stacked alternately, with the iron ions having a unique structure with trigonal bipyramidal 5-coordination (Fig. 10.5). When *h*-$YbFeO_3$ is synthesized by a solvothermal reaction, *h*-$YbFeO_3$ nanocrystals with thin hexagonal plate morphology are obtained, in which the crystal growth in the *c*-axis direction is suppressed. *h*-$YbFeO_3$ can act as a high-performance catalyst for combustion reactions of hydrocarbons [35, 36], and when modified with Mn species, it exhibits higher CO oxidation activity than PGM catalysts [37, 38].

10.3 NO Oxidation and Reduction

10.3.1 Overview

NO_x abatement is becoming increasingly important due to the growing awareness of environmental issues, such as acid rain caused by NO_x emission from thermal power plants or automobiles [39–41]. Although the direct decomposition of NO is thermodynamically favorable, it is kinetically very difficult and often requires temperatures above 600 °C. Therefore, NO reduction to N_2 using hydrocarbons and NH_3 as reductants is widely applied. In contrast, since NO reduction is difficult in an oxygen-rich atmosphere, NO_x-trap materials are sometimes used. In such materials, as NO_2 is more easily adsorbed on the materials' surface than NO, a material with NO oxidation ability in addition to NO_x adsorption ability would be ideal. A typical NO_x-trap catalyst, $Pt/Ba/Al_2O_3$, oxidizes NO to NO_2 at the Pt site and traps NO_2 at the

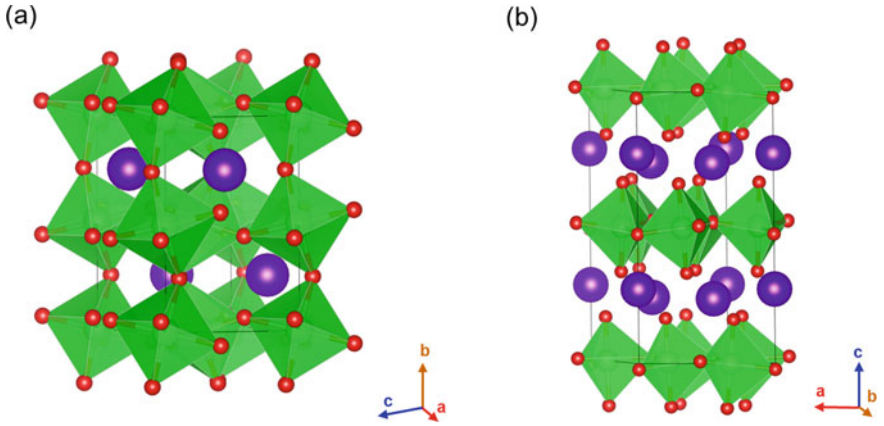

Fig. 10.5 Crystal structure of **a** orthorhombic perovskite $REFeO_3$ with *Pbnm* and **b** hexagonal $REFeO_3$ with $P6_3cm$. Crystal structure is shown as a clear view of the coordination environment of the Fe ion. Purple balls, RE^{3+} ions; green balls, Fe^{3+} ions; red balls; O^{2-} ions

BaO site [39, 42–44]. The NO_x species adsorbed on the catalyst are instantaneously reduced to N_2 by injecting a reductant such as hydrocarbons. Recently, PGM-free metal oxide catalysts that have both NO oxidation and NO_x storage capacity have been reported [45, 46].

In this section, NO_x storage materials involving NO oxidation mechanisms are firstly described, followed by catalyst materials for effective NO reduction based on the MvK-type reaction mechanism. Since most metal oxide catalysts following these reaction mechanisms are related to combustion catalysts [47], the characteristics of their crystal structures are included in Sect. 10.2.

10.3.2 Catalyst Materials

The reaction mechanism for NO oxidation on metal oxides is similar to the previously described MvK mechanism [47]. Many perovskite materials have been reported as catalyst materials for NO oxidation or NO_x storage, such as $La_{1-x}Sr_xCoO_3$ which are known to exhibit a NO oxidation activity comparable to Pt/Al_2O_3 [48, 49]. Ruddlesden-Popper type perovskite $Sr_3Fe_2O_{7-\delta}$, which has a layered structure consisting of a perovskite layer ($SrFeO_{3-\delta}$ layer) and a rock salt layer (SrO layer), shows excellent NO_x storage properties [45]. For these materials, the NO oxidation process involves MvK-type NO oxidation with lattice oxygen, as shown in Eq. (10.3) [50].

$$NO + O_L \rightarrow NO_2 \tag{10.3}$$

The chemical formula of $Sr_3Fe_2O_{7-\delta}$ can be rewritten as $SrO \cdot 2SrFeO_{3-\delta}$, where the SrO layer is incorporated in the structure. In fact, monodentate nitrate (NO_3^-) and ionic nitrate species were observed on the surface of $Sr_3Fe_2O_{7-\delta}$ after NO_x adsorption, suggesting that the SrO layer contributes to the adsorption of NO_x as shown in Eq. (10.4).

$$SrO + 2NO_2 + O^* \rightarrow Sr(NO_3)_2 \tag{10.4}$$

The oxygen source (O*) in Eq. (10.4) is either lattice oxygen species or oxygen species produced by the disproportionation of NO_2. Apart from the NO oxidation properties derived from the $SrFeO_{3-\delta}$ layer, $Sr_3Fe_2O_{7-\delta}$ also presents NO_x adsorption properties derived from the SrO layer, resulting in a high NO_x storage capacity (Fig. 10.6).

These materials require reaction temperatures above 250 °C since NO oxidation triggers NO_x adsorption. In contrast, passive NO_x adsorber (PNA) materials, in which Pd species are highly dispersed in zeolite materials such as ZSM-5 and SSZ, are known to effectively trap NO_x at lower temperatures [51–53]. The NO molecule is adsorbed as it is on the Pd species without any NO oxidation process. However, since the NO-to-Pd ratio is 1, a large amount of Pd loading is essential for high NO_x storage capacity. It has been reported recently that perovskite-type $SrTi_{1-x}Mn_xO_3$ catalysts can efficiently adsorb NO at temperatures below 200 °C even without PGM loading [46].

Regarding NO reduction on metal oxides, the reduction mechanism has been recently proposed according to Eq. (10.5) (Fig. 10.7) [54, 55]:

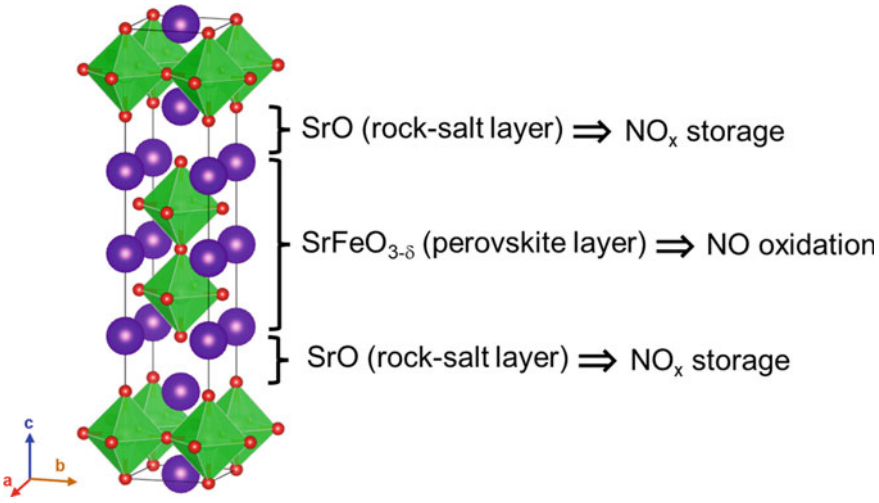

Fig. 10.6 Crystal structure of $Sr_3Fe_2O_{7-\delta}$. Crystal structure is shown as a clear view of the coordination environment of the Fe ions. Purple balls, Sr^{2+} ions; green balls, Fe^{3+} or Fe^{4+} ions; red balls, O^{2-} ions

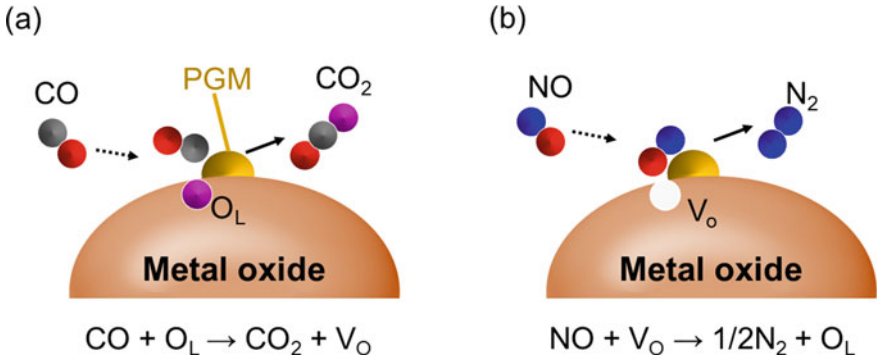

Fig. 10.7 Reaction mechanism of NO–CO reaction based on the MvK mechanism. **a** CO oxidation using lattice oxygen (O_L) and **b** NO reduction using oxygen vacancy (V_o)

$$NO + V_O \rightarrow 1/2N_2 + O_L \tag{10.5}$$

In this reaction, oxygen vacancies are regarded as active sites instead of lattice oxygen that was the case for the MvK mechanism described in Eq. (10.1). During this reduction mechanism, the continuous generation of oxygen vacancy sites is difficult. Therefore, a high temperature or a reducing agent is required for reducing the NO to N_2. For NO reduction processes using CO as a reducing agent, the overall reaction can be written as follows:

$$CO + O_L \rightarrow CO_2 + V_O \tag{10.6}$$

$$NO + V_O \rightarrow N + O_L \tag{10.7}$$

$$N + N \rightarrow N_2 \tag{10.8}$$

A supported PGM catalyst is often used for NO reduction. The reasons are that oxygen vacancy sites can be induced by the PGM loading, and that PGM sites can be used for NO/CO adsorption [38, 55]. For example, in procedures involving automotive exhaust purification, when a very small amount of Pd is supported on the Mn-modified hexagonal $YbFeO_3$, the NO reduction and CO oxidation are drastically enhanced at low temperatures. In this material, the arrangement of Mn cations on the MnO (111) plane is very close to that of Yb cations on the hexagonal $YbFeO_3$ (001); that is, the MnO (111) and $YbFeO_3$ (001) planes are bonded epitaxially. The role of Pd species was theoretically studied by the density functional theory (DFT) using a model in which Pd is supported by the MnO (111). It has been proven that the Pd loading promotes adsorption and dissociation of NO molecules. PGM-free materials have also been developed with Cu and Cr-modified CeO_2 catalysts exhibiting high catalytic activity following the MvK-type NO reduction mechanism [56]. It has

also been found that spinel-type $NiFe_2O_4$ [57, 58] or multicomponent spinel-type catalysts containing four metallic elements (Cu, Ni, Al, Cr) are also effective for NO reduction [59].

10.4 Metal Oxides with Oxygen Storage Performance

10.4.1 Overview

Oxygen storage materials (OSMs) are oxides that can reversibly store and release lattice oxygens in response to variations in temperature and/or oxygen partial pressure. Therefore, this class of materials can be used in various oxygen-related technologies such as exhaust purification in automobiles, chemical looping reactions, and oxygen separation membranes/oxygen sensors [60–64]. OSMs show an interesting crystallographic feature which could be advantageous to rapid and reversible reactions; upon oxygen storage and release, slight structural changes take place. For many transition metal oxides such as spinel-type structures, the crystal structure is composed of close packing O^{2-} ions such that oxygen desorption may significantly deform the lattice framework. However, as described in Sect. 10.2, the packed structures of O^{2-} ions of fluorite-type CeO_2 and perovskite-type oxides are different from those of typical metal oxides. Materials with such characteristic O^{2-} ion-filled structures often store and release oxygen reversibly while maintaining the cationic arrangement. Chemical reactions in which the lattice framework is retained is called "topotactic" [65, 66]. The term "topotactic" is often used for Li intercalation/deintercalation of positive electrode materials in Li-ion secondary batteries. This section introduces the insertion/extraction processes of lattice oxygens based on topotactic reactions.

10.4.2 CeO_2–ZrO_2 Solid Solution

CeO_2–ZrO_2 solid solution (CZ) with fluorite structure is the most well-known oxygen storage material for automotive catalysts [67]. This material reversibly stores and releases lattice oxygens depending on the oxygen concentration in the exhaust gas, contributing to oxygen-pressure control around PGM species that act as active sites. It is known that CZ crystallizes in a fluorite-type structure when the material absorbs oxygen, and the oxygen storage capacity can be adjusted by the mixing ratio of Ce and Zr. For this material, oxygen storage/release proceeds via redox between Ce^{4+} and Ce^{3+}. It can therefore be expected that the oxygen storage capacity depends on the Ce content. However, the oxygen storage capacity of CZ with about 30 mol% Zr is reported to be much higher than that of Zr-free CeO_2. During redox processes, the ionic radii of Ce and Zr are responsible for this phenomenon; when oxygen is released

from the crystal lattice involving a reduction of Ce^{4+} (0.97 Å) to Ce^{3+} (1.14 Å), the lattice volume expands, resulting in local lattice distortions. The presence of smaller Zr^{4+} ions (0.84 Å) at the cation site adjacent to Ce^{3+} mitigates the lattice distortions to form a stable crystal structure containing Ce^{3+} and oxygen deficiencies [68].

During the preparation of CZ exhibiting improved oxygen storage performance, the formation of pyrochlore-type $Ce_2Zr_2O_7$ consisting of an ordered arrangement of Ce and Zr should be formed under a reducing atmosphere at temperatures above 1000 °C [67]. Upon oxygen storage, a phase transition from pyrochlore to fluorite-type structure occurs. Although these two crystal structures are distinct from each other, structural analyses proved that the cationic arrangement is maintained during the phase transition [69]. In other words, topotactic reactions proceed upon oxygen storage and release.

10.4.3 Perovskite and Layered Perovskite Oxides

The topotactic oxygen storage/release also occurs in mixed oxides with perovskite-related structures [70–73]. For this class of materials, since a close-packed structure is formed by A-site cations and O^{2-} ions, the release of oxygen proceeds with minor structural changes. For example, when perovskite-type $SrFeO_{3-\delta}$ is deoxygenated under a hydrogen-containing atmosphere, $Sr_2Fe_2O_5$ with an oxygen-deficient perovskite structure named "brownmillerite-type" is formed without rearrangements at the cation sites. Details of the brownmillerite-type structure are discussed below. However, severe reductive treatments of $SrFeO_{3-\delta}$ at high temperatures lead to structural collapse and the formation of metallic iron. To suppress this structural collapse, a partial substitution of Fe with Ti was reported to be effective by enhancing the structural stability [72].

On the other hand, $Sr_3Fe_2O_{7-\delta}$ with a layered perovskite structure cannot decompose into metallic iron even by severe reductive treatments [66]. The improved phase stability of $Sr_3Fe_2O_{7-\delta}$ is suggested to originate from SrO double layers within the crystal lattice, which would stabilize the oxygen-deficient structure. During oxygen storage/release, the crystal structure remains essentially unchanged with the *I*4*mmm* tetragonal space group (Fig. 10.8). The Fe species in $Sr_3Fe_2O_{7-\delta}$ are Fe^{3+}/Fe^{4+} mixed valent, and the redox between Fe^{3+} and Fe^{4+} is responsible for the oxygen storage and release. The oxygen storage performances are higher than those of Pt/CZ (Fig. 10.9) and the partial replacement of Fe with Ni can improve the oxygen storage capacity of $Sr_3Fe_2O_{7-\delta}$. Structural analysis of deoxygenated $Sr_3(Fe_{0.8}Ni_{0.2})_2O_{7-\delta}$ showed that the reduction of Ni^{3+} to Ni^{2+} proceeds in addition to the reduction of Fe^{4+} to Fe^{3+} [74]. This phenomenon indicates that the Ni^{3+} substitution in $Sr_3Fe_2O_{7-\delta}$ induces the redox activity of the Fe^{3+} site. Indeed, the $Pd/Sr_3(Fe_{0.8}Ni_{0.2})_2O_{7-\delta}$ catalyst shows superior catalytic activity to $Pd/Sr_3Fe_2O_{7-\delta}$ and Pd/CZ for the purification of automotive exhaust gases under fluctuating oxygen concentration, most likely owing to the enhanced oxygen storage capacity of $Sr_3(Fe_{0.8}Ni_{0.2})_2O_{7-\delta}$.

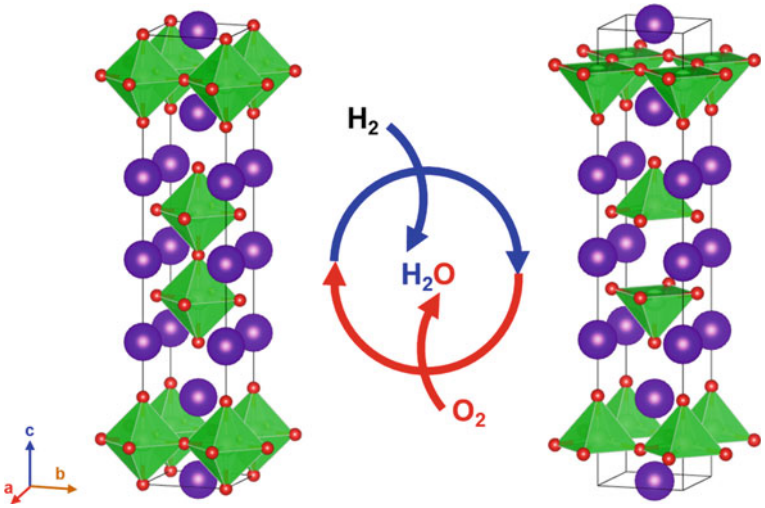

Fig. 10.8 Topotactic oxygen release and storage between $Sr_3Fe_2O_{7-\delta}$ and $Sr_3Fe_2O_6$. Crystal structure is shown as a clear view of the coordination environment of the Fe ions. Purple balls, Sr^{2+} ions; green balls, Fe^{3+} or Fe^{4+} ions; red balls, O^{2-} ions

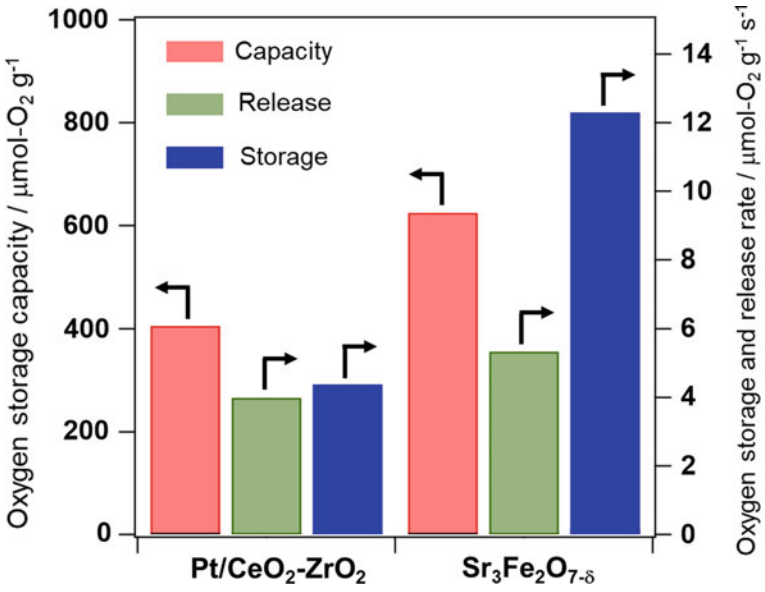

Fig. 10.9 Oxygen storage performances of Pt/CeO_2-ZrO_2 and $Sr_3Fe_2O_{7-\delta}$. These values were obtained using thermogravimetric analysis under H_2–O_2 cycles at 500 °C

10.4.4 Brownmillerite Oxides

As described in Sect. 10.4.3, perovskite oxides are potential OSMs owing to their topotactic oxygen storage/release capability. In the perovskite-type lattice, oxygen deficiencies often form long-range orders, leading to specific crystal phases that enhance structural stability. The brownmillerite (BM)-type structure is a member of the perovskite family with an oxygen deficiency-ordered structure [75]. The BM structure consists of a layered arrangement of tetrahedral BO_4 and octahedral BO_6 units, as illustrated in Fig. 10.10a, in contrast to the perovskite structure that only contains BO_6 units. The general formula for BM oxides is $A_2B_2O_5$ or $ABO_{2.5}$. This structural type is noteworthy owing to the high density of oxygen deficiencies among stable perovskite-derived lattices, that is, 1/6 with respect to the stoichiometric perovskite composition ABO_3. The high density of oxygen deficiencies in BM oxides is beneficial for enhancing their oxygen storage capacity.

Several BM-type OSMs have been reported including $(Sr,Ca)FeO_{2.5}$ and $Sr(Fe,Co)O_{2.5}$ [76–80]. These oxides have attracted attention as potential materials for oxygen absorption that can selectively separate oxygen gas from the atmosphere. This technology is promising as a novel method of oxygen gas production, being more efficient than cryogenic O_2/N_2 distillation and conventional pressure-swing-adsorption using zeolites as N_2 sorbents. Ca_2AlMnO_5 is another BM-type OSM presenting alternating stacking of tetrahedral AlO_4 and octahedral MnO_6 [81]. This oxide stores excess oxygen topotactically and is then transformed into an oxygen-rich form, $Ca_2AlMnO_{5.5}$. The excess oxygen can then be released in a highly reversible manner [82]. The resultant oxygen storage capacity exceeds 3.0 wt%, which is even larger than that of CZ. $Ca_2AlMnO_{5+\delta}$, with excess oxygen amounts δ ranging from 0 to 0.5, is promising in terms of elemental abundance, but its high operating temperatures (~550 °C) are an obstacle to future practical applications. Efforts have been made to lower the operating temperatures, such as Ga-for-Al or Sr-for-Ca substitutions and atomic-defect engineering [83–86].

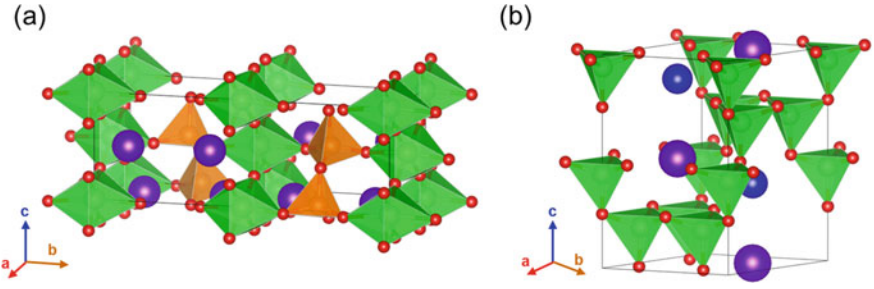

Fig. 10.10 Crystal structure of **a** Ca_2AlMnO_5 with a brownmillerite structure and **b** $YBaCo_4O_7$. Crystal structure is shown as a clear view of the coordination environments of the Mn, Al, and Co ions. Purple balls, Ca^{2+} or Ba^{2+} ions; blue balls, Y^{3+} ions; green balls, Mn^{3+} or Co^{2+} ions; orange balls, Al^{3+} ions; red balls, O^{2-} ions

10.4.5 Other Nonstoichiometric Oxides

Besides the aforementioned CeO_2-based materials and perovskite-related oxides, novel OSMs of other structural types have been extensively studied. Such materials are noteworthy because their unique atomic arrangements could induce characteristic redox behaviors and hence open up the possibility of new areas of applications. In this section, two OSMs, $YBaCo_4O_{7+\delta}$ and $YMnO_{3+\delta}$, are briefly introduced. Noticeably, these oxides have the following common features, which could be crucial factors for high-performance OSMs. (1) Both the oxides contain cationic sites with smaller coordination numbers (CN) than six. Such "coordinatively unsaturated (CN < 6)" sites act as reaction centers for oxygen storage and release. (2) These oxides incorporate excess oxygen topotactically to transform into distinct oxygen-rich forms. Remarkable oxygen storage/release triggered by structural transformations arises even with slight variations in temperature and/or oxygen partial pressure.

$YBaCo_4O_{7+\delta}$ (denoted as "YBCO") has a characteristic structure consisting of a 3D network of corner-sharing CoO_4 tetrahedra, as illustrated in Fig. 10.10b [87]. The corner-sharing framework favors excess-oxygen incorporation. Upon oxygen intake, a part of the CoO_4 tetrahedra transforms into CoO_6 octahedra, leading to large oxygen nonstoichiometry ranging $0 \leq \delta \leq 1.5$ [88, 89]. The oxygen storage/release processes are highly reversible, being controlled by both temperature and oxygen partial pressure. The maximum oxygen storage capacity reaches 4.2 wt%, corresponding to $\Delta\delta = 1.5$ [90]. This value is much larger than that for CZ, making this oxide a promising candidate for high-performance OSM. YBCO works at relatively low temperatures of 300–400 °C in air, and such low operating temperatures are crucial for this oxide to be applied to oxygen-gas production [91]. It should also be pointed out that YBCO shows compositional flexibility, and its oxygen storage characteristics can be widely controlled by chemical substitutions [92].

Oxygen-stoichiometric $YMnO_3$ crystallizes in a hexagonal structure consisting of an alternate stacking of corner-shared MnO_5 trigonal-bipyramids and layers of edge-shared YO_7 polyhedra. This structure is essentially identical to that of *h*-$YbFeO_3$ shown in Fig. 10.5b. This oxide can incorporate excess oxygen into interstitial positions in the MnO_5 layer, resulting in the oxygen-rich form [93]. Upon oxygen intake, various oxygen-rich phases appear in the $YMnO_{3+\delta}$ system (denoted as "YMO") depending on the amount of excess oxygen (δ). These phases are labeled as Hex1 (space group: $R3c$) with $\delta \approx 0.28$, Hex2 ($Pca2_1$) with $\delta \approx 0.41$, and Hex3 ($P6_3mc$) with $\delta \approx 0.45$ [94, 95]. YMO exhibits remarkable oxygen storage/release even at 250 °C or lower, with the maximum oxygen storage capacity reaching 2.5 wt%. The large oxygen storage capacity and low operating temperature ensure that YMO can be a promising OSM. Although YMO is effective as a material for oxygen-gas production, its sluggish oxygen storage/release kinetics are an obstacle to practical applications. To address this issue, various material tailoring protocols were implemented, and partial substitutions of lanthanoids at the Y site have proven effective. Materials with larger lanthanoids, such as $Sm_{0.25}Y_{0.75}MnO_{3+\delta}$ and $Ce_{0.15}Tb_{0.15}Y_{0.70}MnO_{3+\delta}$, were found to show enhanced oxygen storage kinetics at low temperatures [96, 97].

10.5 CH_4 Conversion: Oxidative Coupling of Methane

10.5.1 Overview

Concerns regarding the depletion of natural carbon resources have increased interest in developing ways to effectively utilize methane. Methane is the primary component of natural gas and is the most promising alternative to petroleum. However, methane is a chemically stable molecule with no functional groups, limiting its use to simple combustion for mobility and energy generation. The oxidative coupling of methane (OCM) to C_2 hydrocarbons, such as C_2H_6 and C_2H_4, is a possible route for facile conversion into commodity chemicals [98, 99]:

$$CH_4 + 1/4O_2 \rightarrow 1/2C_2H_6 + 1/2H_2O \quad \Delta H = -89 \text{ kJ mol}^{-1} \tag{10.9}$$

$$CH_4 + 1/2O_2 \rightarrow 1/2C_2H_4 + H_2O \quad \Delta H = -141 \text{ kJ mol}^{-1} \tag{10.10}$$

OCM is a fascinating reaction that is direct, exothermic, and unaffected by thermodynamic constraints. However, to date, no economically feasible process has been established. The reason for this is the absence of suitable catalysts with high C_2 yields (>30%) and long-term durability to meet the practical requirements. The deep oxidation of methane to CO and CO_2 hinders OCM, causing the deterioration of the C_2 selectivity.

10.5.2 Existing Potential Catalysts and OCM Reaction Mechanism

Since the pioneering work [100] of Keller and Bhasin in the 1980s, approximately 2300 reports on OCM have been published. Statistical analysis of the literature data on OCM catalysts suggests several key factors that positively affect the OCM catalytic activity [101]. Catalysts containing alkali, alkali-earth, and rare-earth metals tend to show high catalytic activity. In fact, Li-doped MgO (Li/MgO) [102] and a composite consisting of manganese oxides and sodium tungstates on silica support ($Mn\text{-}Na_2WO_4/SiO_2$) [103, 104] are known to be OCM-active. Unfortunately, both catalysts face technical drawbacks: in long-term operations, they suffer from deactivation due to the vaporization of alkali metals. Regarding the practical application of OCM technology, alternative concepts for catalyst development may help improve the catalytic performance, as reported recently.

The catalytic mechanism of OCM has been extensively investigated. Previous studies have indicated that the formation of C_2 hydrocarbons predominantly involves the gas-phase association of methyl radicals ($\cdot CH_3$) generated at oxygen sites on the catalyst surface [105, 106]. This finding implies that methane activation, that is,

the hydrogen abstraction reaction by the catalyst, is one of the dominating factors affecting OCM activity. Several research groups have reported the importance of the electronic state of oxygen species on the catalyst surface. However, there is no concrete view of the role of such oxygen species, and the activation factors of highly active OCM catalysts are not completely understood.

10.5.3 Recent Progress in the Development of Complex Metal Oxide Catalysts

The aforementioned Mn-Na_2WO_4/SiO_2 catalyst is promising because of its relatively high catalytic activity; typically, C_2 yields are larger than 25% [103, 104]. Nevertheless, the primary activation factor for OCM is still debated owing to the chemical/structural complexity, causing difficulties in further improving its catalytic performance. To overcome this obstacle, single-phase oxides that contain multiple elements seem noteworthy. Single-phase catalysts provide well-defined active sites that are advantageous for mechanistic studies. On the lookout for novel OCM catalysts, few studies have been conducted based on such a strategy, and most of the previous works have focused on perovskite-type oxides [99]. Wang et al. characterized three model $La_2B_2O_7$ compounds with Ti^{4+}, Zr^{4+}, and Ce^{4+} at the B site to prove the phase structure-OCM activity relationship [107]. $La_2Ti_2O_7$, $La_2Zr_2O_7$, and $La_2Ce_2O_7$ crystallize in perovskite-related, pyrochlore, and defective fluorite structures, respectively. The OCM activity followed the order: $La_2Ce_2O_7 > La_2Zr_2O_7 > La_2Ti_2O_7$. The authors suggested that superoxide O_2^- is the active oxygen species, and that the structural type influences the concentration of O_2^- anions, emphasizing the importance of the crystallographic viewpoint.

Matsumoto et al. recently discovered the high OCM activity of crystalline Li_2CaSiO_4 (Fig. 10.11) [108]. The C_2 selectivity and CH_4 conversion reached 77.5% and 28.3%, respectively, at 750 °C with a feed gas ratio of $CH_4/O_2 = 4/1$. In addition, Li_2CaSiO_4 showed stable OCM performance in a durability test over 50 h without phase decomposition and compositional changes. The significant OCM activity of this catalyst is likely to originate from a combination of multiple cations in the crystal lattice; the local coordination around oxygen would give a dual effect of strong basicity and lattice stability, leading to simultaneous enhancements of the CH_4 conversion and C_2 selectivity. Notably, Li_4SiO_4 and Li_4GeO_4 were also found to be OCM-active, with performances comparable to Li_2CaSiO_4 [109]. The high OCM performance of these catalysts is believed to originate from the crystallographic similarities to Li_2CaSiO_4, where every oxygen site is surrounded by one Si/Ge atom and multiple Li atoms, which fulfill the OCM activation factors.

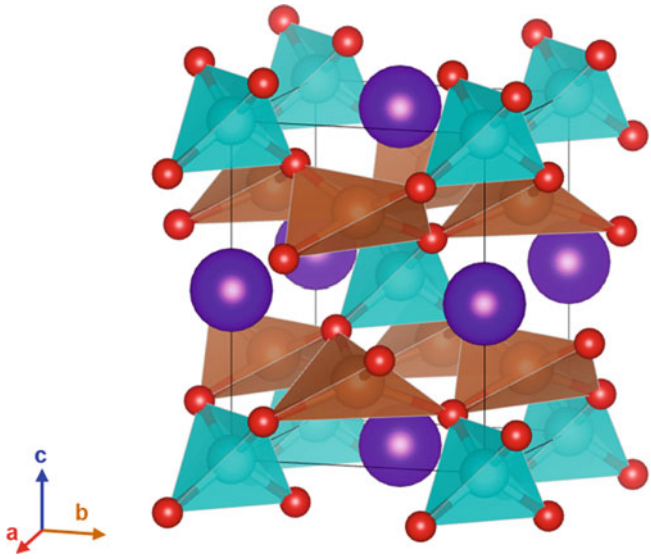

Fig. 10.11 Crystal structure of Li_2CaSiO_4. Crystal structure is shown as a clear view of the coordination environments of the Li and Si ions. Purple balls, Ca^{2+} ions; brown balls, Li^{+} ions; blue balls, Si^{4+} ions; red balls, O^{2-} ions

References

1. Getsoian A, Theis JR, Paxton WA, Lance MJ, Lambert CK. Remarkable improvement in low temperature performance of model three-way catalysts through solution atomic layer deposition. Nat Catal. 2019;2(7):614.
2. Farrauto RJ, Deeba M, Alerasool S. Gasoline automobile catalysis and its historical journey to cleaner air. Nat Catal. 2019;2(7):603.
3. Misumi S, Yoshida H, Hinokuma S, Sato T, Machida M. A nanometric Rh overlayer on a metal foil surface as a highly efficient three-way catalyst. Sci Rep. 2016;6:29737.
4. Yoshida H, Kakei R, Kuzuhara Y, Misumi S, Machida M. A comparative study on TWC reactions over Rh thin films and supported Rh nanoparticles under lean conditions. Catal Today. 2019;332:245.
5. Ueda K, Tsuji M, Ohyama J, Satsuma A. Tandem base-metal oxide catalyst: superior NO reduction performance to the Rh catalyst in NO–C_3H_6–CO–O_2. ACS Catal. 2019;9(4):2866.
6. Royer S, Duprez D, Can F, Courtois X, Batiot-Dupeyrat C, Laassiri S, Alamdari H. Perovskites as substitutes of noble metals for heterogeneous catalysis: dream or reality. Chem Rev. 2014;114(20):10292.
7. Babier Jr. J, Duprez D. Reactivity of steam in exhaust gas catalysis I. Steam and Oxygen/steam conversions of carbon monoxide and of propane over PtRh catalysts. Appl Catal B: Environ. 1993; 3:61.
8. Royer S, Duprez D. Catalytic oxidation of carbon monoxide over transition metal oxides. ChemCatChem. 2011;3(1):24.
9. Hirvi JT, Kinnunen TJ, Suvanto M, Pakkanen TA, Norskov JK. CO oxidation on PdO surfaces. J Chem Phys. 2010;133(8): 084704.
10. Li Y, Yu Y, Wang J-G, Song J, Li Q, Dong M, Liu C-J. CO oxidation over graphene supported palladium catalyst. Appl Catal B: Environ. 2012;125:189.

11. Hosseini M, Barakat T, Cousin R, Aboukaïs A, Su BL, De Weireld G, Siffert S. Catalytic performance of core-shell and alloy Pd–Au nanoparticles for total oxidation of VOC: the effect of metal deposition. Appl Catal B: Environ. 2012;111–112:218.
12. Mars P, van Krevelen DW. Oxidations carried out by means of vanadium oxide catalysts. Chem Eng Sci. 1954;3:41.
13. Wang C, Gu X-K, Yan H, Lin Y, Li J, Liu D, Li W-X, Lu J. Water-mediated Mars-Van Krevelen Mechanism for CO oxidation on Ceria-supported single-atom Pt1 catalyst. ACS Catal. 2016;7(1):887.
14. Carlotto S, Natile MM, Glisenti A, Paul JF, Blanck D, Vittadini A. Energetics of CO oxidation on lanthanide-free perovskite systems: the case of Co-doped $SrTiO_3$. Phys Chem Chem Phys. 2016;18(48):33282.
15. Montini T, Melchionna M, Monai M, Fornasiero P. Fundamentals and catalytic applications of CeO_2-based materials. Chem Rev. 2016;116(10):5987.
16. Artini C. Rare-earth-doped ceria systems and their performance as solid electrolytes: a puzzling tangle of structural issues at the average and local scale. Inorg Chem. 2018;57(21):13047.
17. Yao HC, Yao YFY. Ceria in automotive exhaust catalysts I oxygen storage. J Catal. 1984;86:254.
18. Hosokawa S, Nogawa S, Taniguchi M, Utani K, Kanai H, Imamura S. Oxidation characteristics of Ru/CeO_2 catalyst. Appl Catal A: Gen. 2005;288(1–2):67.
19. Hosokawa S, Taniguchi M, Utani K, Kanai H, Imamura S. Affinity order among noble metals and CeO_2. Appl Catal A: Gen. 2005;289(2):115.
20. Lykaki M, Pachatouridou E, Carabineiro SAC, Iliopoulou E, Andriopoulou C, Kallithrakas-Kontos N, Boghosian S, Konsolakis M. Ceria nanoparticles shape effects on the structural defects and surface chemistry: implications in CO oxidation by Cu/CeO_2 catalysts. Appl Catal B: Environ. 2018;230:18.
21. Delimaris D, Ioannides T. VOC oxidation over $CuO–CeO_2$ catalysts prepared by a combustion method. Appl Catal B: Environ. 2009;89(1–2):295.
22. Delimaris D, Ioannides T. VOC oxidation over $MnO_x–CeO_2$ catalysts prepared by a combustion method. Appl Catal B: Environ. 2008;84(1–2):303.
23. Liotta LF, Ousmane M, Di Carlo G, Pantaleo G, Deganello G, Boreave A, Giroir-Fendler A. Catalytic removal of toluene over $Co_3O_4–CeO_2$ mixed oxide catalysts: comparison with Pt/Al_2O_3. Catal Lett. 2008;127(3–4):270.
24. Trovarelli A, Llorca J. Ceria catalysts at nanoscale: how do crystal shapes shape catalysis? ACS Catal. 2017;7(7):4716.
25. Wang W-W, Yu W-Z, Du P-P, Xu H, Jin Z, Si R, Ma C, Shi S, Jia C-J, Yan C-H. Crystal plane effect of ceria on supported copper oxide cluster catalyst for CO oxidation: importance of metal-support interaction. ACS Catal. 2017;7(2):1313.
26. Voorhoeve RJH, Johnson JDW, Remeika JP, Gallagher PK. Perovskite oxides: materials science in catalysis. Science. 1977;195:7.
27. Tanaka H, Misono M. Advances in designing perovskite catalysts. Curr Opin Solid State Mater Sci. 2001;5:381.
28. Peña MA, Fierro JLG. Chemical structures and performance of perovskite oxides. Chem Rev. 2001;101(7):1981.
29. Zhu J, Li H, Zhong L, Xiao P, Xu X, Yang X, Zhao Z, Li J. Perovskite oxides: preparation, characterizations, and applications in heterogeneous catalysis. ACS Catal. 2014;4(9):2917.
30. Xie X, Li Y, Liu ZQ, Haruta M, Shen W. Low-temperature oxidation of CO catalysed by Co_3O_4 nanorods. Nature. 2009;458:746.
31. Tian Z-Y, Tchoua Ngamou PH, Vannier V, Kohse-Höinghaus K, Bahlawane N. Catalytic oxidation of VOCs over mixed Co–Mn oxides. Appl Catal B: Environ. 2012;117–118:125.
32. Faure B, Alphonse P. Co–Mn-oxide spinel catalysts for CO and propane oxidation at mild temperature. Appl Catal B: Environ. 2016;180:715.
33. Dong C, Qu Z, Qin Y, Fu Q, Sun H, Duan X. Revealing the highly catalytic performance of spinel $CoMn_2O_4$ for toluene oxidation: involvement and replenishment of oxygen species using in situ designed-TP techniques. ACS Catal. 2019;9(8):6698.

34. Nishimura T, Hosokawa S, Masuda Y, Wada K, Inoue M. Synthesis of metastable rare-earth-iron mixed oxide with the hexagonal crystal structure. J Solid State Chem. 2013;197:402.
35. Hosokawa S, Jeon HJ, Iwamoto S, Inoue M. Synthesis of rare earth iron-mixed oxide nanoparticles by solvothermal methods. J Am Ceram Soc. 2009;92(12):2847.
36. Hosokawa S, Jeon HJ, Inoue M. Thermal stabilities of hexagonal and orthorhombic $YbFeO_3$ synthesized by solvothermal method and their catalytic activities for methane combustion. Res Chem Intermed. 2011;37(2–5):291.
37. Hosokawa S, Masuda Y, Nishimura T, Wada K, Abe R, Inoue M. Catalytic properties of Mn-modified hexagonal $YbFeO_3$: noble-metal-free combustion catalysts. Chem Lett. 2014;43(6):874.
38. Hosokawa S, Tada R, Shibano T, Matsumoto S, Teramura K, Tanaka T. Promoter effect of Pd species on Mn oxide catalysts supported on rare-earth-iron mixed oxide. Catal Sci Technol. 2016;6(21):7868.
39. Roy S, Baiker A. NO_x storage-reduction catalysis: from mechanism and materials properties to storage−reduction performance. Chem Rev. 2009;109(9):4054.
40. Granger P, Parvulescu VI. Catalytic NO_x abatement systems for mobile sources: from three-way to lean burn after-treatment technologies. Chem Rev. 2011;111(5):3155.
41. Liu G, Gao P-X. A review of NO_x storage/reduction catalysts: mechanism, materials and degradation studies. Catal Sci Technol. 2011;1(4):552.
42. Olsson L, Persson H, Fridell E, Skoglundh M, Andersson B. A kinetic study of NO oxidation and NO_x storage on Pt/Al_2O_3 and $Pt/BaO/Al_2O_3$. J Phys Chem B. 2001;105:6895.
43. Mulla S, Chen N, Cumaranatunge L, Blau G, Zemlyanov D, Delgass W, Epling W, Ribeiro F. Reaction of NO and O_2 to NO_2 on Pt: kinetics and catalyst deactivation. J Catal. 2006;241(2):389.
44. Bhatia D, McCabe RW, Harold MP, Balakotaiah V. Experimental and kinetic study of NO oxidation on model Pt catalysts. J Catal. 2009;266(1):106.
45. Tamai K, Hosokawa S, Okamoto H, Asakura H, Teramura K, Tanaka T. NO_x oxidation and storage properties of a Ruddlesden-Popper-type $Sr_3Fe_2O_{7-\delta}$-layered Perovskite catalyst. ACS Appl Mater Interf. 2019;11(30):26985.
46. Yoshiyama Y, Hosokawa S, Tamai K, Kajino T, Yoto H, Asakura H, Teramura K, Tanaka T. NO_x storage performance at low temperature over platinum group metal-free $SrTiO_3$-based material. ACS Appl Mater Interf. 2021;13:29482.
47. Hong Z, Wang Z, Li X. Catalytic Oxidation of Nitric Oxide (NO) over different catalysts: an overview. Catal Sci Technol. 2017;7(16):3440.
48. Peng Y, Si W, Luo J, Su W, Chang H, Li J, Hao J, Crittenden J. Surface tuning of $La_{0.5}Sr_{0.5}CoO_3$ Perovskite catalysts by acetic acid for NO_x storage and reduction. Environ Sci Technol. 2016; 50(12):6442.
49. Kim CH, Qi G, Dahlberg K, Li W. Strontium-doped Perovskites rival platinum catalysts for treating NO_x in simulated diesel exhaust. Science. 2010;327(5973):1624.
50. Tamai K, Hosokawa S, Onishi K, Watanabe C, Kato K, Asakura H, Teramura K, Tanaka T. Dynamics of the lattice oxygen in a Ruddlesden-Popper-type $Sr_3Fe_2O_{7-\delta}$ catalyst during NO oxidation. ACS Catal. 2020;10(4):2528.
51. Chen H-Y, Collier JE, Liu D, Mantarosie L, Durán-Martín D, Novák V, Rajaram RR, Thompsett D. Low temperature NO storage of Zeolite supported Pd for low temperature diesel engine emission control. Catal Lett. 2016;146(9):1706.
52. Ryou Y, Lee J, Cho SJ, Lee H, Kim CH, Kim DH. Activation of Pd/SSZ-13 catalyst by hydrothermal aging treatment in passive NO adsorption performance at low temperature for cold start application. Appl Catal B: Environ. 2017;212:140.
53. Zheng Y, Kovarik L, Engelhard MH, Wang Y, Wang Y, Gao F, Szanyi J. Low-temperature Pd/Zeolite passive NO_x adsorbers: structure, performance, and adsorption chemistry. J Phys Chem C. 2017;121(29):15793.
54. Beppu K, Hosokawa S, Asakura H, Teramura K, Tanaka T. Role of lattice oxygen and oxygen vacancy sites in platinum group metal catalysts supported on $Sr_3Fe_2O_{7-\delta}$ for NO-selective reduction. Catal Sci Technol. 2018;8(1):147.

55. Hosokawa S, Shibano T, Koga H, Matsui M, Asakura H, Teramura K, Okumura M, Tanaka T. Excellent catalytic activity of a Pd-promoted MnO_x catalyst for purifying automotive exhaust gases. ChemCatChem. 2020;12(17):4276.
56. Yoshida H, Yamashita N, Ijichi S, Okabe Y, Misumi S, Hinokuma S, Machida M. A thermally stable Cr–Cu nanostructure embedded in the CeO_2 surface as a substitute for platinum-group metal catalysts. ACS Catal. 2015;5(11):6738.
57. Ueda K, Ang CA, Ito Y, Ohyama J, Satsuma A. $NiFe_2O_4$ as an active component of a platinum group metal-free automotive three-way catalyst. Catal Sci Technol. 2016;6(15):5797.
58. Ueda K, Ohyama J, Satsuma A. Investigation of reaction mechanism of NO–C_3H_6–CO–O_2 reaction over $NiFe_2O_4$ catalyst. ACS Omega. 2017;2(7):3135.
59. Hirakawa T, Shimokawa Y, Tokuzumi W, Sato T, Tsushida M, Yoshida H, Hinokuma S, Ohyama J, Machida M. Multicomponent spinel oxide solid solutions: a possible alternative to platinum group metal three-way catalysts. ACS Catal. 2019;9(12):11763.
60. Beppu K, Demizu A, Hosokawa S, Asakura H, Teramura K, Tanaka T. Pd/$SrFe_{1-x}Ti_xO_{3-\delta}$ as environmental catalyst: purification of automotive exhaust gases. ACS Appl Mater Interf. 2018;10(26):22182.
61. Ozawa M, Kimura M, Isogai A. The application of Ce-Zr oxide solid solution to oxygen storage promoters in automotive catalysts. J Alloys Comp. 1993;193:73.
62. Krzystowczyk E, Haribal V, Dou J, Li F. Chemical looping air separation using a Perovskite-based oxygen sorbent: system design and process analysis. ACS Sustain Chem Eng. 2021;9(36):12185.
63. Bulfin B, Lapp J, Richter S, Gubàn D, Vieten J, Brendelberger S, Roeb M, Sattler C. Air separation and selective oxygen pumping via temperature and pressure swing oxygen adsorption using a redox cycle of $SrFeO_3$ perovskite. Chem Eng Sci. 2019;203:68.
64. Fujita K, Asakura H, Hosokawa S, Teramura K, Kobayashi M, Fujita K, Tanaka T. Oxygen release and storage property of Fe–Al spinel compounds: a three-way catalytic reaction over a supported Rh catalyst. ACS Appl Mater Interf. 2021;13(21):24615.
65. Johnson JW, Johnston DC, Jacobson AJ, Brody JF. Preparation and characterization of vanadyl hydrogen phosphate hemihydrate and its topotactic transformation to vanadyl pyrophosphate. J Am Chem Soc. 1984;106(26):8123.
66. Beppu K, Hosokawa S, Teramura K, Tanaka T. Oxygen storage capacity of $Sr_3Fe_2O_{7-\delta}$ having high structural stability. J Mater Chem A. 2015;3(25):13540.
67. Sugiura M, Ozawa M, Suda A, Suzuki T, Kanazawa T. Development of innovative three-way catalysts containing Ceria-Zirconia solid solutions with high oxygen storage/release capacity. Bull Chem Soc Jpn. 2005;78(5):752.
68. Sugiura M. Oxygen storage materials for automotive catalysts: Ceria-Zirconia solid solutions. Catal Surv Asia. 2003;7:77.
69. Urban S, Djerdj I, Dolcet P, Chen L, Möller M, Khalid O, Camuka H, Ellinghaus R, Li C, Gross S, Klar PJ, Bernd S, Over H. In situ study of the oxygen-induced transformation of Pyrochlore $Ce_2Zr_2O_{7+x}$ to the κ-$Ce_2Zr_2O_8$ phase. Chem Mater. 2017;29(21):9218.
70. Vieten J, Bulfin B, Senholdt M, Roeb M, Sattler C, Schmücker M. Redox thermodynamics and phase composition in the system $SrFeO_{3-\delta}$—$SrMnO_{3-\delta}$. Solid State Ion. 2017;308:149.
71. Vieten J, Bulfin B, Call F, Lange M, Schmücker M, Francke A, Roeb M, Sattler C. Perovskite oxides for application in thermochemical air separation and oxygen storage. J Mater Chem A. 2016;4(35):13652.
72. Demizu A, Beppu K, Hosokawa S, Kato K, Asakura H, Teramura K, Tanaka T. Oxygen storage property and chemical stability of $SrFe_{1-x}Ti_xO_{3-\delta}$ with robust Perovskite structure. J Phys Chem C. 2017;121(35):19358.
73. Beppu K, Hosokawa S, Demizu A, Oshino Y, Tamai K, Kato K, Wada K, Asakura H, Teramura K, Tanaka T. Striking oxygen-release/storage properties of Fe-site-substituted $Sr_3Fe_2O_{7-\delta}$. J Phys Chem C. 2018;122:11186.
74. Beppu K, Hosokawa S, Asakura H, Teramura K, Tanaka T. Efficient oxygen storage property of Sr–Fe mixed oxide as automotive catalyst support. J Mater Chem A. 2019;7(3):1013.

75. Antipov EV, Abakumov A, Istomin SY. Target-aimed synthesis of anion-deficient Perovskites. Inog Chem. 2008;47(19):8543.
76. Miura N, Ikeda H, Tsuchida A. $Sr_{1-x}Ca_xFeO_{3-\delta}$ as a new oxygen sorbent for the high-temperature pressure-swing adsorption process. Ind Eng Chem Res. 2016;55(11):3091.
77. Ikeda H, Tsuchida A, Morita J, Miura N. $SrCo_xFe_{1-x}O_{3-\delta}$ oxygen sorbent usable for high-temperature pressure-swing adsorption process operating at approximately 300 °C. Ind Eng Chem Res. 2016;55(22):6501.
78. Popczun EJ, Tafen DN, Natesakhawat S, Marin CM, Nguyen-Phan T-D, Zhou Y, Alfonso D, Lekse JW. Temperature tunability in $Sr_{1-x}Ca_xFeO_{3-\delta}$ for reversible oxygen storage: a computational and experimental study. J Mater Chem A. 2020;8(5):2602.
79. Yin Q, Kniep J, Lin YS. Oxygen sorption and desorption properties of Sr–Co–Fe oxide. Chem Eng Sci. 2008;63(8):2211.
80. Dou J, Krzystowczyk E, Wang X, Robbins T, Ma L, Liu X, Li F. A- and B-site codoped $SrFeO_3$ oxygen sorbents for enhanced chemical looping air separation. Chemsuschem. 2020;13(2):385.
81. Wright AJ, Palmer HM, Anderson PA, Greaves C. Structures and magnetic ordering in the brownmillerite phases, Sr_2MnGaO_5 and Ca_2MnAlO_5. J Mater Chem. 2002;12(4):978.
82. Motohashi T, Hirano Y, Masubuchi Y, Oshima K, Setoyama T, Kikkawa S. Oxygen storage capability of Brownmillerite-type $Ca_2AlMnO_{5+\delta}$ and its application to oxygen enrichment. Chem Mater. 2013;25(3):372.
83. Motohashi T, Kimura M, Inayoshi T, Ueda T, Masubuchi Y, Kikkawa S. Redox characteristics variations in the cation-ordered perovskite oxides $BaLnMn_2O_{5+\delta}$ (Ln = Y, Gd, Nd, and La) and $Ca_2Al_{1-x}Ga_xMnO_{5+\delta}$ ($0 \leq x \leq 1$). Dalton Trans. 2015;44(23):10746.
84. Tanahashi K, Omura Y, Naya H, Miyazaki K, Saito G, Kunisada Y, Sakaguchi N, Nomura T. Sr-doped $Ca_2AlMnO_{5+\delta}$ for energy-saving oxygen separation process. ACS Sustain Chem Eng. 2021;9:9317.
85. Ling C, Zhang R, Jia H. Quantum chemical design of doped $Ca_2MnAlO_{5+\delta}$ as oxygen storage media. ACS Appl Mater Interf. 2015;7(26):14518.
86. Iseki T, Tamura S, Saito M, Tanabe T, Motohashi T. Tunable oxygen intake/release characteristics of Brownmillerite-type $Ca_2AlMnO_{5+\delta}$ involving atomic defect formations. ACS Appl Mater Interf. 2021;13(45):53717.
87. Valldor M, Andersson M. The structure of the new compound $YBaCo_4O_7$ with a magnetic feature. Solid State Sci. 2002;4:923.
88. Chmaissem O, Zheng H, Huq A, Stephens PW, Mitchell JF. Formation of Co^{3+} octahedra and tetrahedra in $YBaCo_4O_{8.1}$. J Solid State Chem 2008;181(3):664.
89. Karppinen M, Otani HY, Fujita T, Motohashi T, Huang YH, Valkeapää M, Fjellvåg H. Oxygen nonstoichiometry in $YBaCo_4O_{7+\delta}$: large low-temperature oxygen absorption/desorption capability. Chem Mater. 2006;18:490.
90. Räsänen S, Yamauchi H, Karppinen M. Oxygen absorption capability of $YBaCo_4O_{7+\delta}$. Chem Lett. 2008;37(6):638.
91. Motohashi T, Kadota S, Fjellvåg H, Karppinen M, Yamauchi H. Uncommon oxygen intake/release capability of layered cobalt oxides, $REBaCo_4O_{7+\delta}$: Novel oxygen-storage materials. Mater Sci Eng: B 2008; 148 (1–3):196.
92. Parkkima O, Karppinen M. The $YBaCo_4O_{7+\delta}$-based functional oxide material family: a review. Euro J Inorg Chem. 2014;2014(25):4056.
93. Remsen S, Dabrowski B. Synthesis and oxygen storage capacities of hexagonal $Dy_{1-x}Y_xMnO_{3+\delta}$. Chem Mater. 2011;23(17):3818.
94. Klimkowicz A, Świerczek K, Kobayashi S, Takasaki A, Allahyani W, Dabrowski B. Improvement of oxygen storage properties of hexagonal $YMnO_{3+\delta}$ by microstructural modifications. J Solid State Chem. 2018;258:471.
95. Klimkowicz A, Cichy K, Chmaissem O, Dabrowski B, Poudel B, Świerczek K, Taddei KM, Takasaki A. Reversible oxygen intercalation in hexagonal $Y_{0.7}Tb_{0.3}MnO_{3+\delta}$: toward oxygen production by temperature-swing absorption in air. J Mater Chem A 2019; 7(6):2608.

96. Otomo M, Hasegawa T, Asakura Y, Yin S. Remarkable effects of lanthanide substitution for the Y-site on the oxygen storage/release performance of $YMnO_{3+\delta}$. ACS Appl Mater Interf. 2021;13(27):31691.
97. Klimkowicz A, Hashizume T, Cichy K, Tamura S, Świerczek K, Takasaki A, Motohashi T, Dabrowski B. Oxygen separation from air by the combined temperature swing and pressure swing processes using oxygen storage materials $Y_{1-x}(Tb/Ce)_xMnO_{3+\delta}$. J Mat Sci. 2020;55(33):15653.
98. Kondratenko EV, Peppel T, Seeburg D, Kondratenko VA, Kalevaru N, Martin A, Wohlrab S. Methane conversion into different hydrocarbons or oxygenates: current status and future perspectives in catalyst development and reactor operation. Catal Sci Technol. 2017;7(2):366.
99. Liu J, Yue J, Lv M, Wang F, Cui Y, Zhang Z, Xu G. From fundamentals to chemical engineering on oxidative coupling of methane for ethylene production: a review. Carbon Resourc Convers. 2022;5(1):1.
100. Keller GE, Bhasin M. Synthesis of ethylene via oxidative coupling of Methane I. Determination of active catalysts. J Catal. 1982;73:9.
101. Zavyalova U, Holena M, Schlögl R, Baerns M. Statistical analysis of past catalytic data on oxidative methane coupling for new insights into the composition of high-performance catalysts. ChemCatChem. 2011;3(12):1935.
102. Ito T, Lunsford JH. Synthesis of ethylene and ethane by partial oxidation of methane over lithium-doped magnesium oxide. Nature. 1985;25:721.
103. Arndt S, Otremba T, Simon U, Yildiz M, Schubert H, Schomäcker R. $Mn–Na_2WO_4/SiO_2$ as catalyst for the oxidative coupling of methane. What is really known? Appl Catal A: Gen. 2012; 425–426:53.
104. Kiani D, Sourav S, Baltrusaitis J, Wachs IE. Oxidative coupling of methane (OCM) by SiO_2-supported tungsten oxide catalysts promoted with Mn and Na. ACS Catal. 2019;9(7):5912.
105. Iwamatsu E, Moriyama T, Takasaki N, Aika K. oxidative coupling of methane over Na^+- and Rb^+-doped MgO. J Catal. 1988;113:25.
106. Aika K, Fujimoto N, Kobayashi M, Iwamatsu E. Oxidative coupling of methane over various metal oxides supported on strontium carbonate catalysts. J Catal. 1991;127:1.
107. Xu J, Zhang Y, Xu X, Fang X, Xi R, Liu Y, Zheng R, Wang X. Constructing $La_2B_2O_7$ (B = Ti, Zr, Ce) compounds with three typical crystalline phases for the oxidative coupling of methane: the effect of phase structures, superoxide anions, and alkalinity on the reactivity. ACS Catal. 2019;9(5):4030.
108. Matsumoto T, Saito M, Ishikawa S, Fujii K, Yashima M, Ueda W, Motohashi T. High catalytic activity of crystalline lithium calcium silicate for oxidative coupling of methane originated from crystallographic joint effects of multiple cations. ChemCatChem. 2020;12(7):1968.
109. Matsumoto T, Ishikawa S, Saito M, Ueda W, Motohashi T. Studies on activation factors for oxidative coupling of methane over lithium-based silicate/germanate catalysts. Catal Sci Technol. 2022;12(1):75.